ceramics

MDPI

Perspective

Osseoconductive $CaTi_{4-z}Zr_z(PO_4)_6$ Ceramics: Solutions Towards Nonunion, Osteoporosis, and Osteoarthrosis Conditions? †

Robert B. Heimann

Independent Researcher, Am Stadtpark 2A, D-02826 Görlitz, Germany; robert.heimann@ocean-gate.de; Tel.: +49-3581-667851 or +49-151-16647505

† Dedicated to Prof. Dr. Rainer Gadow on the occasion of his retirement as Chair of the Institute of Manufacturing Technologies of Ceramic Components and Composites (IMTCCC), University of Stuttgart, Stuttgart, Germany.

Abstract: Transition (Ti, Zr) metal-substituted calcium hexaorthophosphate $CaTi_{4-z}Zr_z(PO_4)_6$ coatings with an NaSICon structure were deposited by atmospheric plasma spraying (APS) onto Ti6Al4Veli substrates using a statistical design of experiments (SDE) methodology. Several coating properties were determined, including chemical composition, porosity, surface roughness, tensile adhesion strength, shear strength, and solubility in protein-free simulated body fluid (pf-SBF) and TRIS-HCl buffer solution. The biological performance evaluation involved cell proliferation and vitality studies and osseointegration tests of coated Ti6Al4Veli rods intramedullary implanted in sheep femora. After a 6 months observation time, a satisfactory gap-bridging potential was apparent as shown by a continuous, well-adhering layer of newly formed cortical bone. These tests suggest that the coatings possess a suitable osseoconductive potential and present an enhanced expression of bone growth-supporting non-collagenous proteins and cytokines, a high cell proliferation, spreading and vitality, and substantial osseointegration by strong bone apposition. The moderate intrinsic ionic conductivity of $CaTi_{4-z}Zr_z(PO_4)_6$ compounds can be augmented by doping with highly mobile Na^+ or Li^+ ions to levels that suggest their use in electric bone growth stimulation (EBGS) devices, able to treat nonunion (pseudoarthrosis) and osteoporosis, and that may also support spinal stabilisation by vertebral fusion.

Keywords: $CaTi_{4-z}Zr_z(PO_4)_6$ coatings; thermal stability; thermal expansion; compressive stress; solubility; ionic conductivity; cytocompatibility; cell proliferation; bioelectricity; electric bone growth stimulation (EBGS) devices

Citation: Heimann, R.B. Osseoconductive $CaTi_{4-z}Zr_z(PO_4)_6$ Ceramics: Solutions Towards Nonunion, Osteoporosis, and Osteoarthrosis Conditions? *Ceramics* **2024**, *7*, 1964–1981. https://doi.org/10.3390/ceramics7040122

Academic Editor: Frank Kern

Received: 14 November 2024
Revised: 12 December 2024
Accepted: 13 December 2024
Published: 16 December 2024

1. Introduction

During the past 50 years, bioinert and bioactive ceramics have been successfully applied as biocompatible artificial materials aimed at replacing parts or functions of the human body in a safe, economical, mechanically reliable, and physiologically and aesthetically acceptable manner. Foremost among bioactive, i.e., osseoconductive, ceramics, synthetic hydroxylapatite (HAp) is used to coat the stem of hip endoprosthetic implants to improve integration with the surrounding bone, as densified implants for dental root replacement, as material for filling bone cavities, and for constructing skeletal prostheses and bone growth-supporting scaffolds. Acting similarly to biological apatite that forms about 70% of the bony composite structure, synthetic hydroxylapatite is capable of establishing direct chemical bonds with hard tissues and thus, behaves akin to the inorganic constituents of the skeleton of all vertebrates.

Calcium phosphate bioceramics, like any other ceramic material, are inherently brittle, as they do not support dislocation movement to block the propagation of microcracks and crack healing, the essential mechanisms that impart ductility to metals. Instead, ceramics show a deleterious coalescence of microcracks, forming supercritical cracks when put under mechanical load. As a consequence of a very low fracture toughness around 1 $MPa \cdot \sqrt{m}$,

hydroxylapatite compacts cannot be utilised for load-carrying medical devices, but instead, hydroxylapatite is predominately applied as a coating on mechanically superior implants, forming the synergistic union of a ductile but bioinert corrosion-resistant metal substrate overlain by a brittle but bioactive ceramic coating.

The preferred deposition technique of hydroxylapatite coatings for medical application is plasma spraying, approved as the method of choice by the US Food and Drug Administration (FDA) and many other international and national health authorities. However, the extremely high temperature of the plasma plume, in excess of 15,000 K, results in the incongruent melting of hydroxylapatite, associated with the formation of crystalline dehydroxlation (oxyhydroxylapatite, OHAp; oxyapatite, OAp) and decomposition phases (tricalcium phosphate, TCP; tetracalcium phosphate, TTCP; calcium oxide, CaO) as well as amorphous calcium phosphate (ACP). Since some of these phases are highly soluble in an aqueous environment including extracellular fluid (ECF), their presence potentially results in the disintegration of the coating in vivo before successful osseointegration has occurred. In particular, the coating layer formed immediately adjacent to the interface has been found to be amorphous and as such, easily soluble. Hence, it acts as a low-energy fracture path that may lead to early coating failure by chipping, spalling, or even complete delamination.

These disadvantages have caused the search for ceramic materials that provide a higher thermal stability and reduced solubility, while retaining the advantageous biological properties of hydroxylapatite. Transition metal-substituted calcium hexaorthophosphate ceramics with an NaSICon structure of the type $CaTi_{4-z}Zr_z(PO_4)_6$ have come into focus as suitable candidate materials for biomedical application [1–5]. Doping these compounds with highly mobile Na^+ or Li^+ ions enhances their intrinsic ionic conductivity to levels that suggest their application in electric bone growth stimulation (EBGS) devices and as a feasible means to treat osteoporotic and trauma-induced bone maladies by the application of stationary electric fields. The present contribution summarises and extends the work on this type of bioceramic performed by the author and his research group during the last two decades.

2. Crystallographic Structure

Transition metal-substituted calcium hexaorthophosphates obey an NaSICon (Na superionic conductor) structure [6]. Their composition can be described by the general formula A_2B_4 $(XO_4)_6$, where A = Na, K, $Ca_{0.5}$, or lattice vacancies; B = Ti, Zr, Nb, La, or other transition metal atoms of appropriate size; and X = P or Si. NaSICons excel by a very low coefficient of linear thermal expansion [7] and hence, a high thermal shock resistance. Figure 1 shows the unit cell of archetypical $CaTi_4(PO_4)_6$. The $Ti_2(PO_4)_3{}^-$ groups are formed by a 3D network of two $TiO_6{}^{8-}$ octahedra connected through their vertices to three $PO_4{}^{3-}$ tetrahedra. These basic units appear as O_3TiO_3-O_3TiO_3 bands along the c-axis of the hexagonal unit cell. Along the ab plane, these bands are connected by $PO_4{}^{3-}$ tetrahedra. The lattice parameters of $CaTi_4(PO_4)_6$ are reported to be a_0 = 0.838 nm; c_0 = 2.203 nm; V = 1.136 nm^3 [7].

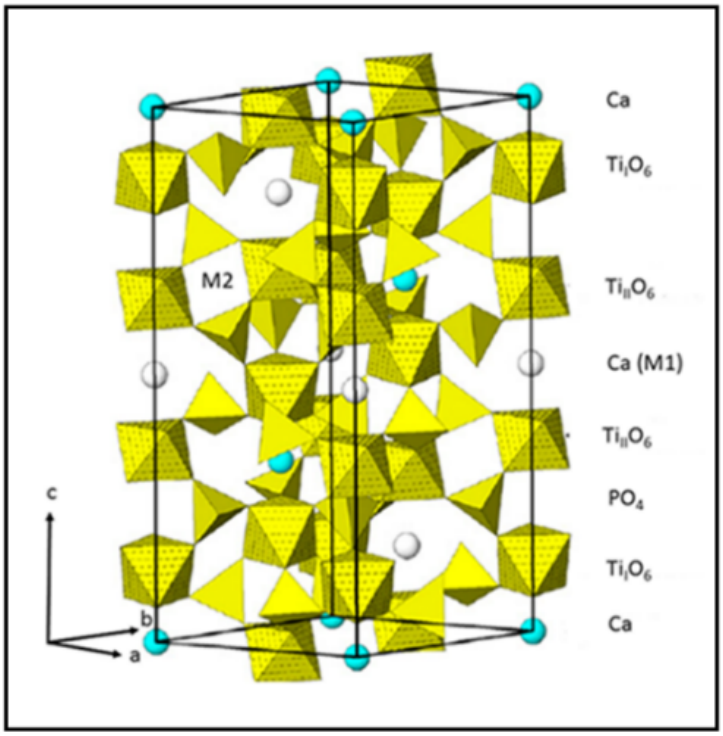

Figure 1. Unit cell of $CaTi_4(PO_4)_6$ with NaSICon structure [4]. © Reproduced with permission from De Gruyter, 2017. All rights reserved.

The structural formula can also be expressed as $[M1^{VI}]$ $[M2^{VI}]$ $[B^{VI}{}_4]$ $[X^{IV}{}_6]O_{24}$, whereby M1 (octahedral symmetry) and M2 (trigonal–prismatic symmetry) are interstitial vacancy sites, either partially or fully occupied by cations. Small highly charged cations such as Ti^{4+} or Zr^{4+} occupy the octahedral B sites, and $SiO_4{}^{4-}$ or $PO_4{}^{3-}$ anions fill the tetrahedral X sites. Many members of the NaSICon group crystallise in the rhombohedral space group $R\bar{3}c$. However, when the monovalent Na^+ or K^+ cations are substituted by a divalent cation such as Ca^{2+}, the symmetry is lowered to $R\bar{3}$. This happens by the ordering of cations and vacancies in the M2 cavities. This configuration leads to the loss of the c-glide plane, since half of the M1 sites are vacant [6]. The smaller tetrahedrally coordinated M2 cavities located between the chains are normally empty and only filled if additional ion contributions are required for charge compensation. These vacancies are at the heart of the structural variability of NaSICons, as well as their intrinsic ionic conductivity [7].

3. Materials and Methods

3.1. Powder Synthesis

Since preliminary solubility tests have shown that the composition with the lowest solubility is $CaTiZr_3(PO_4)_6$, all subsequent studies have concentrated on this composition. Powders for subsequent processing by atmospheric plasma spraying (APS) were synthesized by the solid-state reaction of mixed metal oxides. Stoichiometric amounts of $CaCO_3$ (Merck; 99%), TiO_2 (Riedel-deHaen, Berlin, Germany; 99.5%), and ZrO_2 (ChemPur, Piekary Śląskie, Poland; 99.9%) were mixed with H_3PO_4 (Merck; 85%) and homogenized, dried at 160 °C for 27 h, ground, cold isostatically pressed at 40 MPa to form tablets, sintered, ground again, and classified by sieving. Stepwise sintering was carried out in air at 400 °C (1 h), 800 °C (1 h), 1000 °C (2 h), 1300 °C (72 h), and 1425 °C (1 h).

Critical for synthesis success are a heating rate of 10 °C/min applied during sintering, an overall strict temperature control, and the type of the phosphorus source. For example, the use of a phosphorus source other than H_3PO_4, such as $(NH_4)_2HPO_4$, was found to result in the increased formation of undesired by-products such as rutile (TiO_2), baddeleyite

(ß-ZrO_2), and zirconium diphosphate (ZrP_2O_7). Since ZrO_2 reacts only sluggishly during synthesis, $ZrOCl_2$ was used as a zirconium carrier on a trial basis. However, it must be ensured that the hydrogen chloride released by the hydrolysis of $ZrOCl_2$ can escape sufficiently quickly during drying to prevent it from becoming incorporated into the crystal lattice of the target compound. Frequently, in addition to the desired crystalline $CaTiZr_3(PO_4)_6$ phase, a TiO_2-deficient phase, $CaTi_{0.5}Zr_3(PO_4)_6$, was found as a sintered product. The missing TiO_2 preferentially precipitated as rutile at the grain boundaries of the polycrystalline product.

3.2. Coating Deposition

Near phase-pure $CaTiZr_3(PO_4)_6$ powders (grain size ranges +45–70 µm and +25–45 µm) were deposited on Ti6Al4Veli (ISO 5832-3; HWN Titan GmbH, Mönchengladbach, Germany) substrates (50 × 20 × 2 mm^3) and rods (diameter 12 mm, length 130 mm) by atmospheric plasma spraying (PT-M1000, Plasma-Technik Wohlen, Switzerland, in conjunction with a Sulzer-Metco F4 plasmatron, Winterthur, Switzerland). To increase the adhesion of the coating, the metallic substrates were mechanically roughened by blasting with corundum grit (0.5–1 mm grain size; compressed air 4 bar, blasting angle 75°, distance 100 mm) and then cleaned ultrasonically in Tickopur™ (Bandelin electronic GmbH, Berlin, Germany). To determine the influence of the variation in the intrinsic plasma spray parameters on the coating properties, a two-level statistical Plackett–Burman screening design [8] (sample size N = 12, number of variables p = 11) was applied with factor levels as follows: X_1: plasma energy 35 and 25 kW, X_2: argon flow rate 50 and 40 standard litres per minute (slpm), X_3: hydrogen flow rate 12 and 6 slpm, X_4: powder carrier gas flow rate 6 and 3 slpm, X_5: powder feed rate at 40 and 80% of maximum of the rotation of the powder plate and at 20 and 60% of maximum of the stirrer rotation of the powder hopper, X_6: spray distance 120 and 80 mm, X_7: powder grain size +45–70 and +25–45 µm, X_8 to X_{11}: empty 'dummy' parameters used to estimate the mean standard deviation of the factor effects and thus, the minimum factor significance limits [MIN] (see Ref. [2]).

3.3. Coating Characterisation

The phase composition of the deposited coatings was examined by X-ray diffractometry (D 5000, Siemens, Munich, Germany) and by EDX (SEM JEOL 6400, Tokyo, Japan). The coating porosity was measured by the Archimedes method, and the pore distribution functions were obtained by SEM image analysis (Image C, Intronic GmbH, Dresden, Germany). The ten-point roughness R_z of the coatings was measured with an electrical stylus instrument (Mitutoyo Surftest SV 500; Mitutoyo Deutschland GmbH, Neuss, Germany) and evaluated according to EN ISO 3274:1998-04. The adhesive pull strength according to DIN EN 582:1994 was determined with a universal testing device (Heckert FPZ 100/1, Tamm, Germany). Shear strength was assessed following a non-standardised test developed by Metco Inc., Westbury, NY, USA, in 1963.

3.4. Solubility

The solubilities of the $CaTi_{4-z}Zr_z(PO_4)_6$ powders and coatings deposited on Ti6Al4V substrates (20 × 20 × 2 mm^3) were assessed in protein-free simulated body fluid (pf-SBF) and TRI-HCl buffer at pH = 7.4. The samples were agitated in an incubator at 37 ± 0.5 °C for 120 h. The eluates were analysed for their phosphorus content by atomic absorption spectrometry (AAS) and by inductively coupled plasma spectrometry (ICPS) for their content of Ca^{2+}, Ti^{4+} and Zr^{4+} ions.

3.5. Cellular Proliferation and Vitality Test

To determine cytocompatibility, in vitro tests were conducted with bone marrow cells (BMCs) derived from adult rats. The cells were incubated for 24 h in 500 µL α-MEM (Eagle's minimal essential medium) + 15% foetal bovine serum + 10^{-8} mole dexamethasone + 50 µg/mL ascorbic acid + 10 nmol ß–glycerophosphate, and seeded with a density of $3{\cdot}10^4$ cells/cm^2 onto the surface of $CaTiZr_3(PO_4)_6$ disks sintered for 72 h at 1300 °C. After a cell culture period of 2 weeks, the cells were fixed and stained with Giemsa stain (Biomol GmbH, Hamburg, Germany). Thermanox™ cell cover slips (ThermoFisher Scientific, Waltham, MA, USA) were used as a control. The quality of cell proliferation and cell vitality was graded as follows: class I—areas without cells, isolated cells, or cell detritus; class II—areas with loose reticular cell associations; class III—areas covered with a thick layer of cells; class IV—nodular centres with a multilayered cell formation.

3.6. Biological Performance Testing in a Sheep Model

$CaTiZr_3(PO_4)_6$-coated Ti6Al4V rods (diameter 12 mm, length 130 mm) were intramedullary implanted in the femora of two adult sheep (approx. 60 kg weight) under general (55 mg midazolam i.v., 700 mg ketamine i.v.) and epidural regional anaesthesia (4 mL Carbostesin 0.5%, Astra, Södertälje, Sweden) after the intramuscular injection of 1400 mg ketamine and 30 mg midazolam.

After a 6 months observation period, the sheep were sacrificed by injecting 15 mg dormicum i.m., 700 mg ketamine i.m., and 20 mL T61 i.v. (Hoechst-Roussel vet., Budapest, Hungary). The distal femora were explanted and stored in an alcoholic solution with ascending concentrations (70–100%) and xylene substitute (Histoclear, Schandau, Germany) for 3 days, embedded in methylmethacrylate (MMA), and, after polymerisation, cut into blocks with a diamond circular saw. The blocks were glued to glass plates with a Technovit® 4000 (Kulzer GmbH, Hanau, Germany) and then ground and re-glued onto glass slides with a Technovit® 7210 VLC. After cutting them to a thickness of 100 µm with a diamond circular saw, grinding, and polishing, the thus obtained histological sections were stained with toluidine blue (Merck GmbH, Darmstadt, Germany) and examined under a light microscope. All animal experiments were conducted in full compliance with the existing ethical regulations and procedures of the Federal Republic of Germany (FRG) and the European Union (EU).

4. Results and Discussion

An evaluation of the response functions of the statistical experimental design yielded the coating property ranges [2,3] shown in Table 1.

Table 1. Mechanical properties and solubility of $CaTiZr_3(PO_4)_6$ coatings obtained by a statistical Plackett–Burman [8] screening design.

Property	Dimension	Minimum	Average ± s.d.	Maximum
Coating thickness	µm	43.0	183.0 ± 76.0	312.0
Porosity	vol%	10.4	17.0 ± 4.4	23.7
Adhesion strength	MPa	3.4	7.7 ± 4.3	17.3
Surface roughness	µm	46.2	54.7 ± 8.3	69.5
Shear strength	MPa	0.2	3.6 ± 4.4	12.8
Solubility in SBF *	mg/l	1.0	3.2 ± 1.7	5.2

* total solubility = $\Sigma[cCa^{2+} + c(PO_4)^{3-}]$.

In general, thinner coatings show enhanced adhesion and shear strengths and reduced solubility. However, the rather wide spread of the obtained property values signals a need for further optimisation of the plasma spray parameters by statistical design strategies beyond the limited resolution of the exploratory screening design used in this study. This

applies in particular to the coating adhesion to the Ti alloy substrate surface, the rather low value of which calls for stringent parameter optimisation strategies.

4.1. Thermal Stability

Atmospheric plasma spraying of $CaTiZr_3(PO_4)_6$ powders produced coatings with an adhesion to Ti6Al4V substrates near or slightly exceeding the minimum strength of 15 MPa stipulated by the ISO 13779-2 norm [9] (Table 1). However, incongruent melting with considerable thermal decomposition occurred, forming zirconium pyrophosphate (ZrP_2O_7), rutile (TiO_2), and baddeleyite (β-ZrO_2), as well as several sub-stoichiometric phosphorus-depleted structures [2,10,11]. This is demonstrated in the cross-sectional images of plasma-sprayed coatings shown in Figure 2A–C.

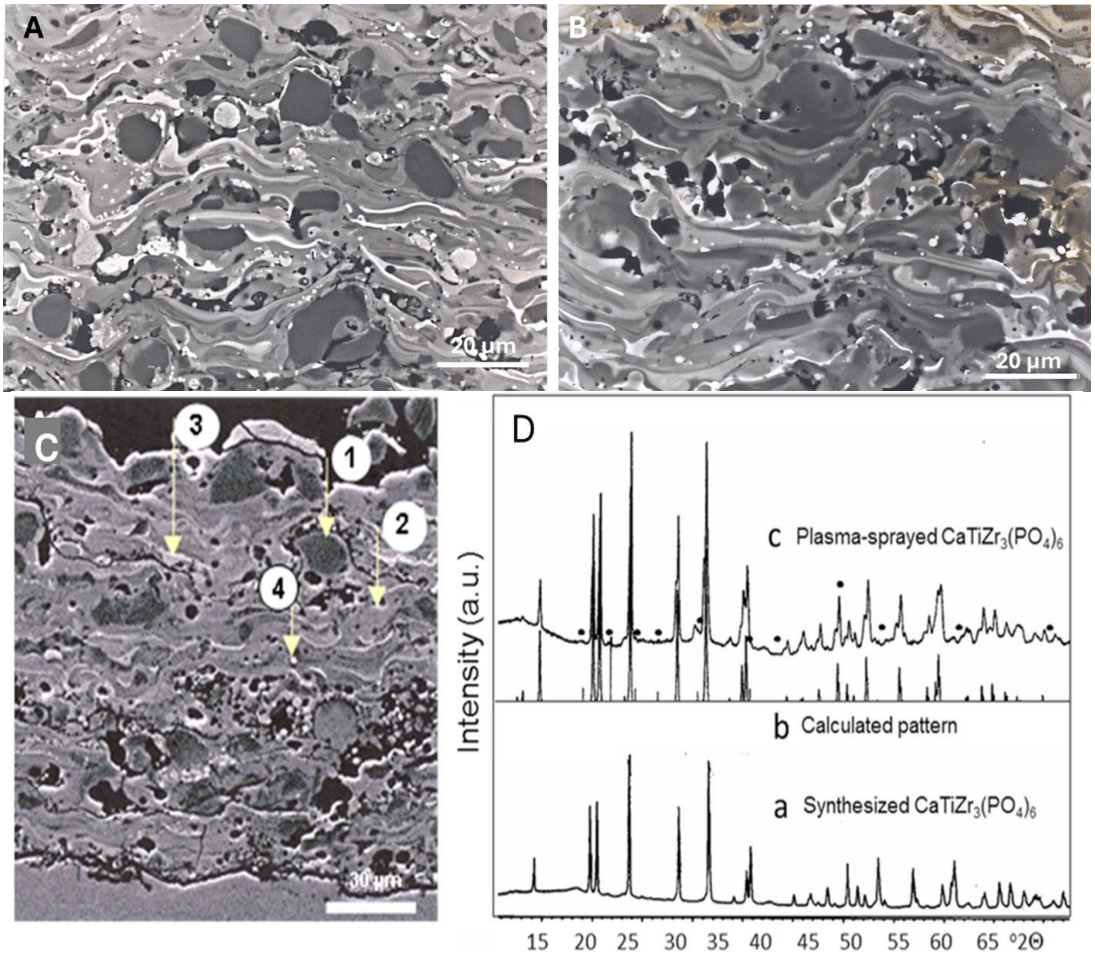

Figure 2. Typical cross-sections of atmospheric plasma-sprayed $CaZr_4(PO_4)_6$ (**A**) and $CaTi_2Zr_2(PO_4)_6$ (**B**) coatings on Ti6Al4V substrates [10]. Dark: target compounds; medium grey: phosphorus-depleted phases; white: rutile and/or ß-zirconia exsolutions (spheres) as well as ZrP_2O_7 (worm-like flow-marks) (see **C**,**D**). © Images courtesy of Dr Guido Reisel, Oerlikon Metco WOKA GmbH, Barchfeld, Germany. (**C**): Cross-section of a plasma-sprayed $CaTiZr_3(PO_4)_6$ coating on a Ti6Al4V substrate [11]. Phase 1: target compound; phase 2: $Ca(Ti,Zr)_{4.5}O_{4.6}(PO_4)_{3.6}$; phase 3. $Ca(Ti,Zr)_{4.2}O_{6.85}(PO_4)_{1.7}$; phase 4: ß-$ZrO_2$. Note that the decomposition phases 2 and 3 are strongly depleted in phosphorus. (**D**): X-ray diffraction pattern of as-synthesised $CaTiZr_3(PO_4)_6$ (a), calculated pattern (b), and plasma-sprayed coating (c). The peaks marked with dots can be assigned to ZrP_2O_7. © Reprinted with permission from Wiley-VCH, Weinheim, Germany, 2010.

Figure 3 shows cross-sectional images of typical plasma-sprayed coatings with an average porosity of 17 vol% (dark areas), thought to promote the easy ingrowth of bone

cells when used as osseoconductive coatings on implants. Of particular importance is the absence of a microcrack network, a feature that signals the tight adhesion of the coating to the titanium alloy substrate, shown by a continuous interface. This provides resistance to coating chipping or delamination during loading with shear stress-imposed forces. The few cracks shown in Figure 3B are thought to be generated during sample preparation for electron microscopical examination.

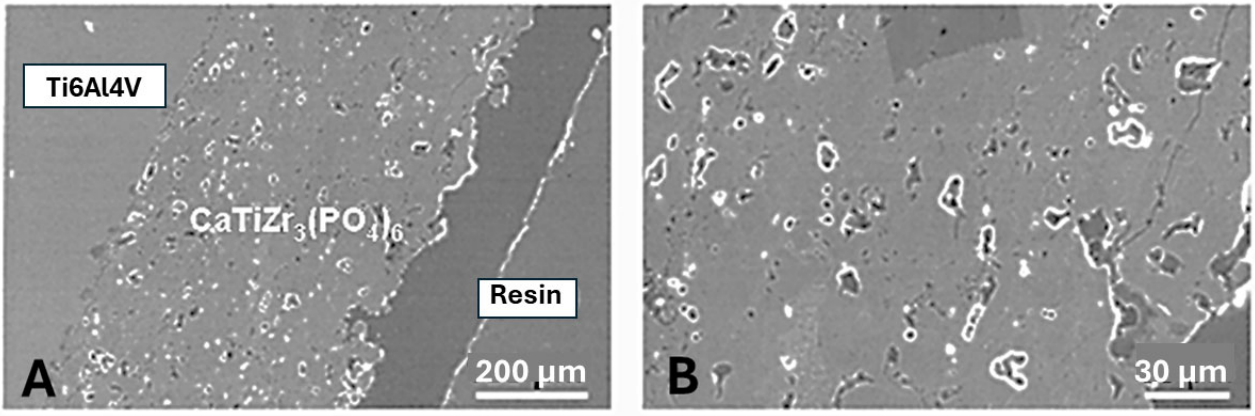

Figure 3. (**A**,**B**) Cross-sectional images of plasma-sprayed $CaTiZr_3(PO_4)_6$ coatings on a Ti6Al4V substrate at different magnifications. Plasma power 30 kW, argon flow rate 45 standard litres per minute (slpm), hydrogen flow rate 8 slpm, powder carrier gas (argon) flow rate 4.5 slpm, spray distance 100 mm, powder grain size +25–45 µm [11]. © Reprinted with permission from Wiley-VCH, Weinheim, Germany, 2010.

4.2. Thermal Expansion

$CaTiZr_3(PO_4)_6$ ceramics excel by a strongly anisotropic low coefficient of thermal expansion parallel to the c-axis at $\alpha = 0.92(1)\cdot10^{-6}$ K^{-1} and moderate thermal expansion parallel to the a-axis at $\alpha = 5.09(0)\cdot10^{-6}$ K^{-1} [7], in stark contrast to hydroxylapatite ($\alpha > 11 \cdot 10^{-6}$ K^{-1}) [12]. Consequently, the lower coefficient of the linear thermal expansion of $CaTiZr_3(PO_4)_6$ ceramics compared to hydroxylapatite predicts the development of compressive coating stresses according to eq. 1 when applied to Ti6Al4V ($\alpha = 8.6 \cdot 10^{-6}$ K^{-1} [13]) implant surfaces, in contrast to the tensile stresses generated in the presence of hydroxylapatite coatings. These advantageous compressive stresses promote a tight and lasting coating adhesion to Ti alloy implant surfaces, whereas tensile stresses were found to generate cracks perpendicular to the coating surface. These cracks may reach down to the implant surface, allowing the penetration of ECF in vivo, which may lead to the preferential dissolution of the layer of amorphous calcium phosphate (ACP) formed during the first stage of the coating process.

The principal equation governing the generation of thermal coating stress σ_c can be expressed by the equation

$$\sigma_c = \{\frac{E_c(\alpha_c - \alpha_s)\Delta T}{1 - \nu_c} + [\frac{1 - \nu_s}{E_s}]d_c/d_s\} \quad (1)$$

where E is Young's modulus of elasticity, α is the coefficient of thermal expansion, ΔT is the temperature difference, ν is the Poisson's number, and d is the thickness. The subscripts c and s refer to coating and substrate, respectively. Since at given values of ν and E the thermal coating stress σ_c increases with increasing coating thickness d_c, the risk of spalling is much higher in thick coatings than in thin ones. Moreover, depending on the sign of $(\alpha_c - \alpha_s)$, the thermal stress can be either tensile ($\alpha_c > \alpha_s$) or compressive ($\alpha_c < \alpha_s$). Quenching and thermal stresses, combined with the complicated solidification process of the coating, are the two main contributors to the overall residual stress. Whereas during deposition the substrate is usually at some elevated temperature, post-depositional cooling

to room temperature generates additional stress by a thermal mismatch proportional to the differences in the thermal expansion coefficients of the coating and the substrate, as well as the intrinsic elastic moduli (see Equation (1)). An advantageous reduction in deleterious thermal stresses and thus, an enhancement in the adhesive strength of this novel type of coating is highly likely when the appropriate parameter optimisation during plasma spraying is carried out [5].

4.3. Coating Porosity

The average porosity of the coatings was determined to be $p = 17.0 \pm 4.4\%$ (N = 12). The pore-size distribution was found to be unimodal in thin coatings (<60 µm), with a preferential mean pore diameter of 10.8 µm (Figure 4A), but multimodal in thicker coatings (≥180 µm), with frequency maxima at pore diameters of 12, 24, and 36 µm (Figure 4B).

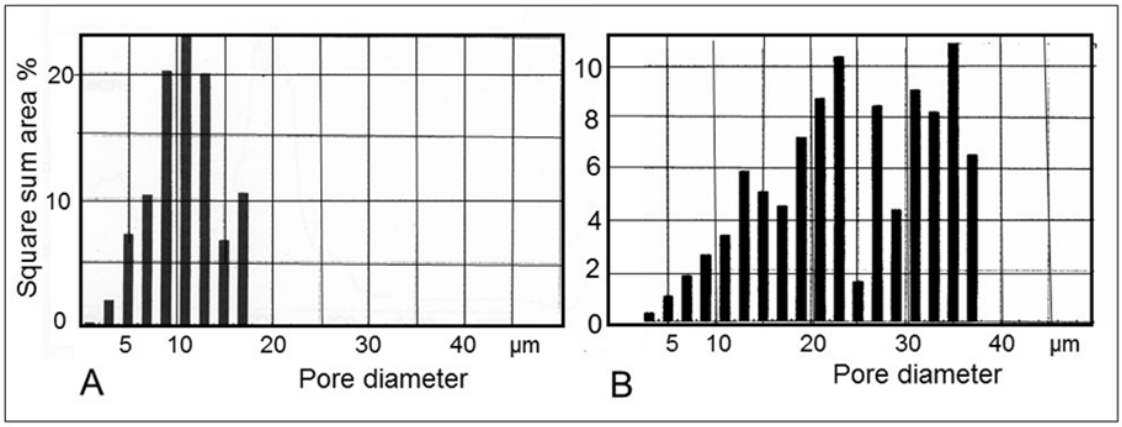

Figure 4. Pore-size distribution of plasma-sprayed $CaTiZr_3(PO_4)_6$ coatings. (**A**) Unimodal distribution, mean porosity $p = 10.8$ vol%. (**B**) Multimodal distribution, mean porosity $p > 15.5$ vol% [14]. © Reprinted with permission from Wiley-VCH, Weinheim, Germany, 2015.

Higher porosities that support the ingrowth of bone cells more efficiently could be obtained by advanced deposition techniques such as suspension plasma spraying (SPS) or solution precursor plasma spraying (SPPS) [14].

4.4. Solubility

Calcium (Ti, Zr) hexaorthophosphate ceramics show in vitro solubilities in simulated body fluid (SBF) or 0.2 M TRIS-HCl buffer solution at least one order of magnitude lower than those of hydroxylapatite and, in particular, tricalcium phosphate [11]. Figure 5A shows the experimentally obtained solubilities of hydroxylapatite (A) and tricalcium phosphate (B), as well as $CaTi_{4-z}Zr_z(PO_4)_6$ phases with various substitution ratios z (C to G) [15]. The solubilities of the $CaTi_{4-z}Zr_z(PO_4)_6$ compounds appear to be incongruent, i.e., the concentration of $[PO_4]^{3-}$ measured in solution is considerably higher than that of Ca^{2+}, in contrast to hydroxylapatite (A).

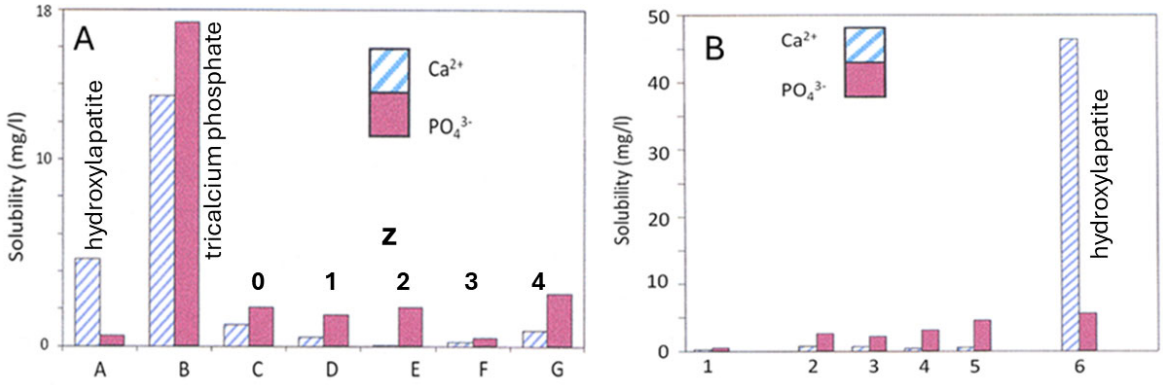

Figure 5. (**A**): Solubilities of calcium (titanium, zirconium) hexaorthophosphates with different Ti/Zr ratios (C–G) compared to hydroxylapatite (A) and tricalcium phosphate (B) in protein-free simulated body fluid at 37 °C and pH 7.4 [11]. C: $CaTi_4(PO_4)_6$; D: $CaTi_3Zr(PO_4)_6$; E: $CaTi_2Zr_2(PO_4)_6$; F: $CaTiZr_3(PO_4)_6$; G: $CaZr_4(PO_4)_6$. (**B**): Solubilities of plasma-sprayed $CaTiZr_3(PO_4)_6$ (F in (**A**)) in 0.2.M TRIS-HCl buffer at 37 °C and pH 7.4 [11]. 1: as-synthesised; 2–5: coatings with different sets of plasma spray parameters; 6: plasma-sprayed hydroxylapatite. © Reprinted with permission from Wiley-VCH, Weinheim, Germany, 2015.

The lowest solubility was found for $CaTiZr_3(PO_4)_6$. Consequently, subsequent studies were conducted with this composition, plasma-sprayed with varying parameters (2–5) as shown in Figure 5B. The solubilities of the coatings, although higher than that of the as-synthesised starting powder (1), were much lower than that of plasma-sprayed hydroxylapatite (6). The average solubility Σ [cCa^{2+} + $cPO_4{}^{3-}$] of the $CaTi_{4-z}Zr_z(PO_4)_6$ compounds was determined to be 3.17 ± 1.67 mg/L (2 to 5), as compared to that of plasma-sprayed hydroxylapatite, which presents an average total solubility of ~50 mg/L (6). The concentrations of Ti^{4+} and Zr^{4+} ions were found to be in the range of their detection limits.

4.5. Ionic Conductivity

As opposed to metals with high concentrations of mobile electrons or electron holes that support strong electrical conductivity, most ceramics are either dielectrics, i.e., electrical insulators that can be polarised by an applied electric field, or semiconductors. In the case of a dielectric, instead of charge-carrying electrons, the displacement of charges contributes predominately to conductivity.

The origin of ionic conductivity in transition metal-substituted calcium hexaorthophosphates with an NaSICon structure is grounded on their atomic arrangement, which forms a hexagonal skeleton of space group $R\bar{3}c$ or $R\bar{3}$ with large structural vacancy sites (see Section 2). The vacancy sites with octahedral symmetry (M1) are occupied by small cations with the coordination number [6] such as Ti^{4+} or Zr^{4+}. The vacancies with trigonal–prismatic symmetry (M2) are either empty as in $Nb^{5+}{}_4(PO_4)_6$ or occupied by two-valent ions as in $Ca^{2+}Ti_4(PO_4)_6$ (Figure 1) or by three-valent ions as in $La^{3+}{}_{0.67}Ti_4(PO_4)_6$. These vacancies account for the structural variability of the NaSICon family, as well as their intrinsic ionic conductivity. It should be mentioned in passing that presently much research effort is being expanded on enhancing the ionic conductivity of Al- or rare earth-substituted $Li_2Ti_4(PO_4)_6$ ceramics for improved lithium-based batteries [16].

Doping with highly mobile ions such as Na^+, Li^+, or rare-earth ions enhances the ionic conductivity of NaSICons. Na^+ ions migrate by hopping [17,18] from one site to its neighbouring vacant site, during which the ions have to overcome a diffusion barrier by squeezing through a triangular 'bottleneck' formed by three O atoms. The size of this bottleneck is critical to the ionic conductivity as it controls the rate of ion migration. Hence, the bulk conductivity can be enhanced by tailoring, i.e., widening, the size of the bottleneck by appropriate ion substitution [19]. Another option is to dope the NaSICon structure

with, instead of Na^+ (Shannon ion radius 102 pm), a smaller ion such as Li^+ (Shannon ion radius 76 pm).

Quantitative data for the ionic conductivity of NaSICons appears to differ considerably depending on the chemical composition and preparation conditions. Silva et al. [20] reported the d.c. conductivity of (undoped) $CaTi_4(PO_4)_6$ to be $\sigma = 4.0 \cdot 10^{-12}$ S·m^{-1}, about 30 times the conductivity of hydroxylapatite. The dielectric permittivity was reported as $\varepsilon = 15.4$ and thus, somewhat higher than that of hydroxylapatite (ε = 10–12). In contrast, Fuentes et al. [21] obtained submicrometric grains of $Na_3Si_2(Zr_{1.88}Y_{0.12})PO_{11.94}$ by the sintering of mechanically activated precursor powders and determined their ionic conductivity to be $\sigma = 2.5 \cdot 10^{-5}$ S·m^{-1}, seven orders of magnitude higher than that reported in Ref. [20]. This relatively high value of electric conductivity can be associated with the high concentration of the charge-carrying Na^+ ions and their higher electric mobility compared to the Ca^{2+} ions in the former structure. These highly mobile Na^+ ions are able to move in response to an outside electric field within the cavities of the unit cell.

More recently, NaSICon compounds with an ionic conductivity as high as $1.2 \cdot 10^{-1}$ S·m^{-1} were synthesised [22]. It was found that the substitution of PO_4^{3-} polyanions by SiO_4^{4-} enhances the ionic conductivity and that the effect of Na content on the ionic conductivity is based preferentially on its function as an activation barrier, rather than through the carrier concentration itself.

4.6. Cytocompatibility

4.6.1. Cell Proliferation and Vitality

In vitro biocompatibility tests with primary rat bone marrow cells revealed substantial cell proliferation, spreading, and vitality in the presence of foetal bovine serum. Table 2 shows the rating of cell proliferation, vitality, and morphology [3]. The slightly higher percentage of classes III + IV, together with the much lower percentage of class I observed on $CaTiZr_3(PO_4)_6$ surfaces compared to the control, suggest the advanced osseogenic potential of the former.

Table 2. Rating of cell proliferation, vitality, and morphology in percentage of area covered [3].

Substrate	Class I	Class II	Class III	Class IV	Classes III + IV	Class (III + IV)/I
$CaTiZr_3(PO_4)_6$	1	24	27	48	75	75
Thermanox™ control	7	27	24	42	66	9.4

Knabe et al. [23] cultured human bone-derived cells (hBDCs) on sintered $CaTi_{4-z}Zr_z(PO_4)_6$ surfaces and tested the expression of various biochemical indicators for cell proliferation and cell vitality, such as enhanced levels of osteocalcin, osteonectin, osteopontin, alkaline phosphatase (ALP), and bone sialoprotein I. Compositions conforming specifically to $CaTiZr_3(PO_4)_6$ showed the maximum osteoblastic differentiation, including a sufficient expression of an array of osteogenic markers, suggesting a high degree of osseoconductive potential. Future studies may involve MTT assays, as well as a live/death cell assessment using fluorescence microscopy.

4.6.2. Implantation Tests

Animal tests revealed that a 150 µm thick $CaTiZr_3(PO_4)_6$ coating applied to Ti6Al4V rods implanted in the femoral medulla of sheep [2,14,24] (Figure 6) and the lateral condyle of dogs [25] induced a strong neoformation of dense cortical bone at a stable interface of implant–bioceramic coating, without the coating delamination sometime observed with hydroxylapatite. Figure 6A shows the bony integration of the implant to be flawless, characterised by the continuous growth of the bone tissue towards the implant body. In the transition to the medullary cavity, the remaining gap to the surrounding cortical bone is filled by direct bone–implant contact (Figure 6B). The left part of the image shows failed bony bridging capability when the distance of the implant from the bone bed is too large.

Only in sections, a thin lamellar covering of the implant is visible at a higher magnification.

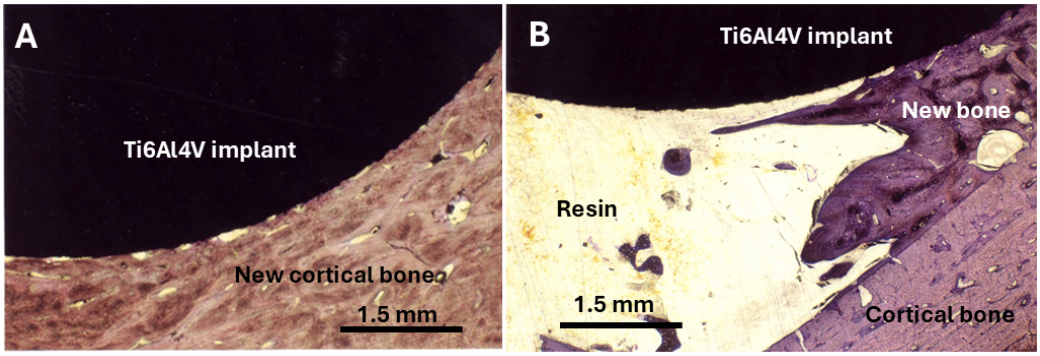

Figure 6. (**A**) Light-optical micrograph of a distal section of a Ti6Al4V rod coated with $CaTiZr_3(PO_4)_6$ and implanted in the femoral medulla of a sheep for six months. (**B**) The gap-bridging potential of newly formed bone (centre right) is reduced when the distance between the coated implant and surrounding cortical bone (bottom right) is increased [2,14]. © Reprinted with permission from Wiley-VCH, Weinheim, Germany, 2015.

It ought to be mentioned that the advantageous bone response observed in the presence of a $CaTiZr_3(PO_4)_6$ coating [2,14] as described above is inconsistent with earlier results of rabbit model studies. Ti alloy cylinders coated with $Ca_{4.5}Zr_{2.25}(PO_4)_6$ were implanted in the distal femoral epiphyses of female chinchilla rabbits, and their bone apposition behaviour was studied in histological sections using light [26] and electron microscopy [27]. In addition to macrophages distributed in the soft tissue at the bone–implant interface, primary trabecular bone had formed that, however, consisted mainly of a non-mineralised bone matrix (osteoid). The reason for the inhibited mineralisation was attributed to the presence of Zr ions that, in the opinion of the authors, negatively influenced the development and function of matrix vesicles [28]. These vesicles are extracellular organelles of 50 to 150 nm size and are believed to play a major role in endochondral matrix mineralisation by delivering their cargo of alkaline phosphatase (ALP) and adenosine triphosphatase (ATP), plus Ca-binding molecules such as annexin and phosphatidyl serine [29], to the plasma membrane of osteoblasts via protein–ligand interaction [30]. The impediment of these functions by Zr ions may prevent the all-important formation of mineralised tissue during osteogenesis, as manifested by the presence of a non-mineralised bone matrix.

In contrast, an earlier study conducted by Szmukler-Moncler et al. [31] obtained different results. They implanted Ti discs coated with $CaZr_4(PO_4)_6$ into the distal epiphyseal parts of canine femora and tibiae and observed a direct and stable contact between implant and bone. After a 9 months observation time, extensive remodelling of osteons had occurred in direct contact with the bioceramic material, without a noticeable resorption of the latter. During fracturing for specimen preparation, separation occurred within the bone but not at the ceramic–bone interface, suggesting very strong bone apposition. This work was indeed a key experiment that established the appropriate in vivo osseoconductive capability and stability of these novel ceramic materials. Similar results have been reported for the growth of bone marrow stromal cells cultured on calcium titanium phosphate microspheres to be used as potential scaffolds for bone reconstruction [32].

4.7. Bone Bioelectricity

The endogenous bioelectrical properties of bone originate from the interaction of osteocyte, osteoblast, and osteoclast cells with the surrounding extracellular matrix (ECM), triggered by biomechanical stimuli arising from routine physical activities [33]. They can be described as a complex overlap of dielectric, piezoelectric, pyroelectric, and ferroelectric effects, together with streaming potential, the osmotic movement of ions separated by cell membranes, and the presence and action of voltage-gated ion channels. Bioelectric

signals arising from the action of these ion channels regulate cell behaviour in terms of numbers (proliferation and apoptosis), positions (orientation and migration), and identities (differentiation) [34]. The activity of ion channels establishes a resting membrane potential, as well as other electric signals.

There is a close interdependence and interaction between the various electroactive and electrosensitive components of bone tissue, including cell membrane potential, voltage-gated ion channels, intracellular signalling pathways, and cell surface receptors, together with various matrix components such as tropocollagen, hydroxylapatite, proteoglycans, and glycosaminoglycans [33]. This interactive crosstalk between the organic and inorganic components of bone controls their electrophysiological properties. Based on the physiological importance of these effects, there is a growing interest in the application of electroactive scaffolds in bone tissue engineering, designed to simulate the natural electrophysiological microenvironment of healthy bone tissue to repair various bone defects [35].

4.8. Acceleration of Bone Growth in the Presence of an Electric Field

Given the plethora of these bone defects, historically there have been many more or less effective medical treatments, going back thousands of years [36]. The growth rate of bone is affected by the presence of materials with different dielectric properties subject to the so-called 'bioelectric phenomenon' [37]. Mechanically triggered electrical charge separation acts as the principal mechanism that drives the remodelling of a broken bone, since the structure and function of growing bone cells and extracellular structures will be influenced by piezoelectric and streaming potentials [38].

Clinical studies have shown that the electrical stimulation of bone with electric fields aligned parallel to the axis of a long bone reduces the time required for endosteal callus remodelling and hence, the healing process [39]. However, since improved bone healing at the negative electrode is accompanied by resorption of bone (osteolysis) at the positive electrode, the concept of the electrical stimulation of bone healing must be approached judiciously to balance these two antagonistic effects. Unfortunately, despite much research performed during the past decades, the origin and function of bioelectric potentials are not known with certainty as yet. Presumably, diffusion gradients, i.e., ionic currents, are established that are able to concentrate polarisable molecules, collagenous proteins, non-collagenous polyanionic proteins, and electrolytes at the trauma site. There is some indication that the concentration of Ca^{2+} ions at the negative electrode is higher than in a non-stimulated bone fracture. Ca^{2+} cations originate from the depolymerisation of mucopolysaccharides and $PO_4{}^{3-}$ anions from the glycogenolysis of phosphate esters by the action of alkaline phosphatase (ALP). The ions initially stored in the mitochondria are released by a change in the potential of the mitochondrial membrane via the cytoplasm and the cell membrane into the extracellular matrix (ECM) [40].

The notion of the acceleration of bone growth by a poled electrical field is strongly supported by more recent research findings that the growth of hydroxylapatite crystals from simulated body fluid is being drastically quickened on negatively polarised dielectric and ferroelectric substrates such as calcium and barium titanates [41]. These experiments suggest that a uniform electric field, rather than localised charges, is the stimulating factor of bone remodelling during the healing process [42]. Although the exact mechanism is still unclear, there is evidence that the growth of bone-like hydroxylapatite in an electric field is accelerated by the reorientation of the dipole moments between O^{2-} and H^{+} of lattice OH^{-} ions in response to the electric polarisation conditions.

Whereas the orientation of the OH^{-} groups of hydroxylapatite requires an outside electric field, it is suggested that $CaTiZr_3(PO_4)_6$ behaves differently, in that spontaneous polarisation may occur owing to charge imbalances within the $TiO_6{}^{8-}$ octahedral groups. This, however, would impart ferroelectric behaviour, which, however, has not been reported hitherto for the NaSICon structure family [12].

In conclusion, electrical (and electromagnetic) fields are thought to play an important role in bone healing by mechanisms similar to mechanical stress application. When a

mechanical load is applied to bone, a strain gradient develops. Subsequent pressure gradients in the interstitial fluid drive fluid through the bone from regions of high to low pressure and thus, expose osteocyte membranes to a flow-related shear stress that generates an endogenous electrical potential. This so-called streaming potential develops when interstitial fluid is driven by a pressure gradient through the lacuno-canalicular network (LCN) of bone [43]. Many details of this effect are still shrouded in mystery, but the application of electrical or electromagnetic fields to the fracture site have been found to mimic the effect of mechanical stress on bone, leading to enhanced bone growth and hence, healing [44]. However, there is a caveat. Although the idea of fixing bone defects by electrical stimulation has a long and colourful pedigree, it still elicits scepticism within the medical community owing to the lack of homogeneity in the trial design, dosage, and consistency of reporting of results [35]. State-of-the-art information on EBGS can be extracted from Refs. [45–47].

4.9. A Proposed Bone Growth Stimulator

Electrical bone growth stimulation (EBGS) is used to promote bone growth and the healing of fractures, including the treatment of nonunion (pseudoarthrosis) or spinal fusions. This can be done by applying an electrical current to the fracture or fusion site.

The positive effect on the well-being of the patient, as well as on the economy of governmental health provision, could be substantial if the recovery time, for example after a total hip arthroplasty (THA) operation, could be reduced by the accelerated healing of the operational trauma site. Speeding up the healing process might be achieved using electric or electromagnetic fields to accelerate bone growth. Such innovative technology could also be applied to construct novel osteosynthetic devices, i.e., surgical fixtures that stabilise and join the ends of fractured bones, such as metal plates, pins, or screws.

Electrical stimulation can be applied either from the outside (non-invasive) or from the inside (invasive) of the body. Invasive electrical bone growth stimulators apply direct currents to the fracture or bone fusion site. However, this solution may not be ideal as it requires an additional surgical operation and may involve the risk of nosocomial infection. Although multiple randomised trials exist to support a variety of bone stimulation modalities, all are limited to primarily radiologic endpoints. Hence, there remains a need to conduct large and definitive trials using patient-oriented outcomes before the universal acceptance of such modalities will occur [44].

Designing and applying a Ti6Al4V/TiO_2/$CaTiZr_3(PO_4)_6$ layered system (Figure 7) could eventually lead to a device with the equivalent circuit of a capacitor, which, by proper poling, could store negative electrical charges close to the interface with the growing bone, thus enhancing the bone apposition rate and presumably, bone density [4].

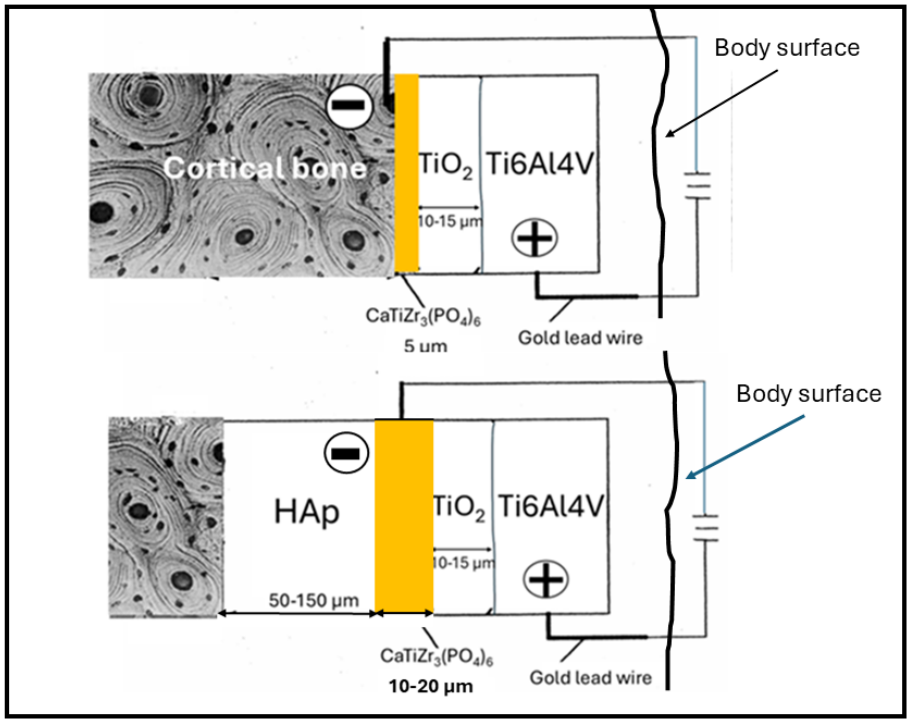

Figure 7. Two possible configurations of invasive electric bone growth stimulation (EBGS) devices based on ion-conducting $CaTiZr_3(PO_4)_6$. (**Top**) without a hydroxylapatite coating, (**bottom**) in the presence of a hydroxylapatite coating. The thin TiO_2 layer acts as a dielectric able to store negative charges close to the interface with bone.

Advanced osseoconductive implant coatings based on transition metal-substituted calcium hexaorthophosphates with solid-state ionic conductivity may be utilised to construct a capacity-coupled invasive electric bone growth stimulator (EBGS) with configurations shown in Figure 7. The advantage of such devices over already existing bone growth stimulators may be seen in providing the intimate contact of a capacity-coupled electric field with the growing bone tissue, as opposed to an externally applied inductivity-coupled electromagnetic field that suffers substantial attenuation when transmitted through the soft tissue that covers the locus of bone growth. To achieve a higher ionic conductivity in Ca(Ti,Zr) hexaorthophosphates, aliovalent doping with highly mobile Na^+ or Li^+ ions will provide a suitable route.

In the past, many EBGS devices have been experimentally explored [47], including invasive direct current electric stimulators (DCESs), non-invasive inductively coupled pulsed electromagnetic field (PEMF) devices, and non-invasive capacitively coupled (CC) devices. Electric power can be delivered by conventional batteries or self-powered piezoelectric (PENG) or triboelectric (TENG) nanogenerators [48–50] that are capable of converting mechanical into electrical energy. Other self-powered energy sources such as photovoltaics and pyroelectrics could potentially be applied in constructing alternate EBGSs.

5. Other Potential Biomedical Applications

Based on their multifunctional advantageous properties, transition metal-substituted calcium hexaorthophosphates may be considered the 'Sleeping Beauty' of osseoconductive coatings for endoprosthetic implants, osteosynthetic fixation devices, and electroactive scaffolds in bone tissue engineering.

The advantageous properties of these novel bioceramics include the following:

- Low solubility;
- Low coefficient of thermal expansion;
- Intrinsic ionic conductivity;
- Tight adhesion to titanium alloy implant surfaces with a continuous interface;
- High osseoconductive potential;
- Enhanced expression of non-collagenous proteins and cytokines;
- High cell proliferation, spreading, and vitality;
- Enhanced osseointegration by strong bone apposition.

However, there are some potential disadvantages that render the application of these novel compounds in need of close scrutiny and further in-depth studies. They include the following:

- Thermal instability owing to incongruent melting;
- Presence of decomposition phases such as ZrO_2 that may be distributed by the lymphatic system throughout the body and may trigger 'particle disease';
- Presence of phosphate-depleted phases with enhanced solubility;
- Presence of Zr^{4+} ions that may negatively influence the development of matrix vesicles and their function.

Since the thermal decomposition of transition metal-substituted calcium hexaorthophosphates is the root cause of all these disadvantages, this impediment could largely be alleviated by non-thermal coating deposition techniques such as sol–gel deposition, pulsed laser deposition, or radio-frequency magnetron sputtering [13]. The deposition of thin $CaTi_4(PO_4)_6$ coatings on Ti alloy substrates by micro arc oxidation (MAO) was reported by Zhao and Wen [51].

In addition, calcium (titanium, zirconium) hexaorthophosphate ceramics with a comparatively low solubility in ECF may potentially be used to coat arthroplastic endoprosthetic implants. Such coatings may be required when, during a total hip arthroplasty (THA) operation involving a replacement of the implant, the adjacent cortical bone matter was previously damaged. This leads frequently to an undesirable geometric configuration of the surrounding cortical bone bed. In this situation, a thin, less resorption-resistant hydroxylapatite coating may not be able to sustain a large-scale bone regeneration process that would exceed the residence time of a thin coating [23]. Consequently, coatings consisting of bioceramics with a higher resorption resistance and potentially better adhesion to the implant surface, such as transition metal-substituted calcium hexaorthophosphates, constitute a novel approach to arthroplastic remedial operations [2,3,31].

6. Concluding Remarks

Transition metal-substituted calcium hexaorthophosphates were found to provide moderately porous and reasonably well-adhering coatings with excellent biocompatibility and osseoconductivity, as well as a low solubility in vivo compared to hydroxylapatite, with its comparatively high solubility. In addition, such compounds attain substantial ionic conductivity when doped with highly mobile ions such as Na^+ or Li^+ that are able to move in response to an outside electric field within the cavities of the crystalline structure. This suggests interesting options to design so-called fourth-generation biomaterials that utilise bioelectric properties for theragnostic purposes [24,52] to manipulate the cellular bioelectric signals required for bone tissue regeneration and to monitor cellular responses to external stimuli, allowing future remote communication with the host tissues. In addition, electrically stimulated bone growth may be achieved, able to successfully treat conditions such as nonunion (pseudoarthrosis) and osteoporosis and support spinal stabilisation by vertebrae fusion. Based on their advantageous properties determined in vitro and the reasonable biomedical performance observed in vivo, osseoconductive $CaTi_{4-z}Zr_z(PO_4)_6$ bioceramics may be rightly considered the 'Sleeping Beauty' of materials for medical applications.

Funding: This research was funded in part by the German Research Foundation (DFG), grant number He 923/9-1/2.

Institutional Review Board Statement: Not applicable.

Data Availability Statement: Data available in publicly accessible repositories at https://doi.org/10.3390/ma12132059; https://doi.org/10.2138/am-2017-6165; and ISBN 978-1-62257-299-1.

Acknowledgments: I am grateful to Kerstin Schneider for synthesising the bioceramic powders, measuring porosities, and determining solubilities, and to Margitta Hengst and Guido Reisel for the plasma-spray coating experiments, all of the Department of Mineralogy, TU Bergakademie Freiberg. I would like to thank Reinhold T. Müller and Nicole Schürmann, formerly of University Hospital Essen, for conducting the animal experiments that were carried out in full compliance with the currently applicable laws in the Federal Republic of Germany. Ulrich Gross, formerly of Klinikum B. Franklin, Freie Universität Berlin, and Georg Berger, formerly of Bundesanstalt für Materialforschung und-prüfung (BAM), Berlin, have contributed valuable advice and discussions. Christine Knabe-Ducheyne, Philipps University Marburg, formerly of Klinikum B. Franklin, Freie Universität Berlin, performed the cell proliferation and vitality tests.

Conflicts of Interest: The author declares no conflicts of interest.

References

1. Lugscheider, E.; Berger, G.; Knepper, M.; Sicking, R.; Nyland, A. Plasma-sprayed coatings of calcium titanium phosphate: A new generation of bioactive coatings. In *Bioceramics*; Wilson, J., Hench, L.L., Greenspan, D., Eds.; Pergamon Press: Oxford, UK, 1995; Volume 8, pp. 317–322.
2. Heimann, R.B. In vitro-und in vivo-Verhalten von osteokonduktiven plasmagespritzten Ca-Ti-Zr-Phosphat-Beschichtungen auf Ti6Al4V-Substraten [In vitro and in vivo performance of osseoconductive plasma-sprayed Ca-Ti-Zr phosphate coatings on Ti6Al4V substrates]. *BIOmaterialien* **2006**, *7*, 29–37.
3. Heimann, R.B. Transition metal-substituted calcium orthophosphates with NaSICon structure: A novel type of bioceramics. In *Calcium Phosphate: Structure, Synthesis, Properties, and Applications*; Nova Science Publishers: New York, NY, USA, 2012; pp. 363–379, ISBN 978-1-62257-299-1.
4. Heimann, R.B. Calcium (Ti, Zr) hexaorthophosphate bioceramics for electrically stimulated biomedical implant devices: A position paper. *Am. Min.* **2017**, *102*, 2170–2179. [CrossRef]
5. Heimann, R.B. Plasma-sprayed bioactive ceramic coatings with high resorption resistance based on transition metal-substituted calcium hexaorthophosphates. *Materials* **2019**, *12*, 2059. [CrossRef] [PubMed]
6. Alamo, J. Chemistry and properties of solids with the [NZP] skeleton. *Solid State Ion.* **1993**, *63–65*, 547–561. [CrossRef]
7. Senbhagaraman, S.; Guru Row, T.N.; Umarji, A.M. Structural refinement using high-resolution powder X-ray diffraction data of $Ca_{0.5}Ti_2P_3O_{12}$, a low-thermal-expansion material. *J. Mater. Chem.* **1993**, *3*, 309–316. [CrossRef]
8. Plackett, R.L.; Burman, J.P. The design of optimum multifactorial experiments. *Biometrika* **1946**, *33*, 305–325. [CrossRef]
9. *ISO 13779-2*; Implants for Surgery: Hydroxyapatite. Part 2: Coatings of Hydroxyapatite. ISO: Geneva, Switzerland, 2008.
10. Reisel, G. Entwicklung von HVOF- und APS-Gespritzten Biokeramischen Schichten für die Endoprothetik. [Development of HVOF- and APS-Sprayed Coatings for Endoprosthetic Applications]. Master's Thesis, RWTH Aachen, Aachen, Germany, September 1996.
11. Heimann, R.B. *Classic and Advanced Ceramics, from Fundamentals to Applications*; Wiley-VCH Verlag GmbH & Co. KGaA: Weinheim, Germany, 2010; ISBN 978-3-527-32517-7.
12. Miyazaki, H.; Ushiroda, I.; Itomura, D.; Hirashita, T.; Adachi, N.; Ota, T. Thermal expansion of hydroxyapatite between −100 °C and 50 °C. *Mater. Sci. Eng. C* **2009**, *29*, 1463–1466. [CrossRef]
13. Boyer, R.; Welsch, G.; Collings, E.W. *Materials Properties Handbook: Titanium Alloys*; ASM International: Materials Park, OH, USA, 1994.
14. Heimann, R.B.; Lehmann, H.D. *Bioceramic Coatings for Medical Implants. Trends and Techniques*; Wiley-VCH Verlag GmbH & Co. KGaA: Weinheim, Germany, 2015; pp. 428–429, ISBN 978-3-527-33743-9.
15. Schneider, K.; Heimann, R.B.; Berger, G. Plasma-sprayed coatings in the system CaO-TiO_2-ZrO_2-P_2O_5 for long-term stable endoprostheses. *Mater. Werkst.* **2001**, *32*, 166–171. [CrossRef]
16. Lu, Z.X.; Chen, Z.L.; Wang, M.Q.; Wan, Y.; Yan, J.; Chen, S.; Shen, Y.; Yan, Z.; Wang, D. Roles of lithium aluminum titanium phosphate in lithium batteries. *ACS Appl. Energ. Mater.* **2023**, *6*, 2541–2549. [CrossRef]
17. Sahimi, M. Hopping conductivity of heterogeneous materials. In *Applications of Percolation Theory*; Applied Mathematical Sciences; Springer: Cham, Switzerland, 2023; p. 213.
18. Kang, S.D.; Snyder, G.J. Charge-transport model for conducting polymers. *Nat. Mater.* **2017**, *16*, 252–257. [CrossRef]
19. Li, C.; Li, R.; Liu, K.N.; Si, R.; Zhang, Z.; Hu, Y. NaSICon: A promising solid electrolyte for solid-state sodium batteries. *Interdiscip. Mater.* **2022**, *1*, 396–416. [CrossRef]
20. Silva, C.C.; Graça, M.P.F.; Valente, M.A.; Sombra, A.S.B. AC and DC conductivity analysis of hydroxyapatite and titanium calcium phosphate formed by dry ball milling. *J. Non-Cryst. Solids* **2006**, *352*, 1490–1491. [CrossRef]

21. Fuentes, R.O.; Figueiredo, F.M.; Soares, M.R.; Marques, F.M.B. Submicrometric NASICON ceramics with improved electrical conductivity obtained from mechanically activated precursor. *J. Eur. Ceram. Soc.* **2005**, *25*, 455–462. [CrossRef]
22. Wang, J.Y.; He, T.J.; Yang, X.C.; Cai, Z.; Wang, Y.; Lacivita, V.; Kim, H.; Ouyang, B.; Ceder, G. Design principles for NASICON super-ionic conductors. *Nat. Comm.* **2023**, *14*, 5210. [CrossRef]
23. Knabe, C.; Berger, G.; Gildenhaar, R.; Klar, F.; Zreiqat, H. The modulation of osteogenesis in vitro by calcium titanium phosphate. *Biomaterials* **2004**, *25*, 4911–4919. [CrossRef]
24. Heimann, R.B. (Ed.) *Materials for Medical Application*; Walter de Gruyter GmbH: Berlin, Germany, 2020; ISBN 978-3-11-061919-5.
25. Itiravivong, P.; Promasa, A.; Laiprasert, T.; Techapongworachai, T.; Kuptniratsaikul, S.; Thanakit, V.; Heimann, R.B. Comparison of tissue reaction and osteointegration of metal implants between hydroxyapatite/Ti alloy coat: An animal experimental study. *J. Med. Assoc. Thail.* **2003**, *86*, S422–S430.
26. Gross, U.; Müller-Mai, C.; Berger, G.; Ploska, U. The tissue response to a novel calcium zirconium phosphate ceramic. *Key Eng. Mater.* **2003**, *240/242*, 629–632. [CrossRef]
27. Gross, U.; Müller-Mai, C.; Berger, G.; Ploska, U. Do calcium zirconium phosphate ceramics inhibit mineralization? *Key Eng. Mater.* **2004**, *254/256*, 635–638. [CrossRef]
28. Bernstein, A.; Nöbel, D.; May, H.O.; Göbel, F.; Berger, G.; Ploska, U.; Gildenhaar, R.; Brandt, J. Inhibition of mineralization by a calcium zirconium phosphate coating. *J. Biomed. Mater. Res. B* **2008**, *86*, 422–429. [CrossRef]
29. Anderson, H.C. Matrix vesicles and calcification. *Curr. Rheumatol. Rep.* **2003**, *5*, 222–226. [CrossRef]
30. Ansari, S.; de Wildt, B.W.M.; Vis, M.A.M.; de Korte, C.E.; Ito, K.; Hofmann, S.; Yuana, Y. Matrix vesicles: Role in bone mineralization and potential use as therapeutics. *Pharmaceuticals* **2021**, *14*, 289. [CrossRef] [PubMed]
31. Szmukler-Moncler, S.; Daculsi, G.; Delécrin, J.; Passuti, N.; Deudon, C. Calcium-metallic phosphates: A new coating biomaterial? *Adv. Biomater.* **1992**, *10*, 377–383.
32. Barrias, C.C.; Ribeiro, C.C.; Lamghari, M.; Miranda, C.S.; Barbosa, M.A. Proliferation, activity, and osteogenic differentiation of bone marrow stromal cells cultured on calcium titanium phosphate microspheres. *J. Biomed. Mater. Res. A* **2005**, *72*, 57–66. [CrossRef] [PubMed]
33. Heng, B.C.; Bai, Y.Y.; Li, X.C.; Meng, Y.; Lu, Y.; Zhang, X.; Deng, X. The bioelectric properties of bone tissue. *Anim. Model Exp. Med.* **2023**, *6*, 120–130–130. [CrossRef]
34. Cohen, D.J.; Nelson, W.J.; Maharbiz, M.M. Galvanotactic control of collective cell migration in epithelial monolayers. *Nat. Mater.* **2014**, *13*, 409–417. [CrossRef]
35. Isaacson, B.M.; Bloebaum, R.D. Bone bioelectricity: What have we learned in the past 160 years? *J. Biomed. Mater. Res. A* **2010**, *95*, 1270–1279. [CrossRef]
36. Basford, J.R. A historical perspective of the popular use of electric and magnetic therapy. *Arch. Phys. Med. Rehabil.* **2001**, *82*, 1261–1269. [CrossRef]
37. Fukada, E. On the piezoelectric effect in bone. *J. Phys. Soc. Jpn.* **1957**, *12*, 1159–1162. [CrossRef]
38. Bassett, C.A.L.; Becker, R.O. Generation of electric potential by bone in response to mechanical stress. *Science* **1962**, *238*, 1063–1064. [CrossRef]
39. Berry, J.L.; Geiger, J.L.; Moran, J.M.; Skraba, J.S.; Greenwald, A.S. Use of tricalcium phosphate or electrical stimulation to enhance bone-porous implant interface. *J. Biomed. Mater. Res.* **1986**, *20*, 65–77. [CrossRef]
40. Rubin, B.; Saffir, A. Calcification and the ground substance: Precipitation of calcium phosphate crystals from a nutrient gel. *Nature* **1970**, *225*, 78–80. [CrossRef] [PubMed]
41. Yamashita, K.; Oikawa, N.; Umegaki, T. Acceleration and deceleration of bone-like crystal growth on ceramic hydroxyapatite by electric poling. *Chem. Mater.* **1996**, *8*, 2697–2700. [CrossRef]
42. Calvert, P.; Mann, S. The negative side of crystal growth. *Nature* **1997**, *386*, 127–128. [CrossRef]
43. Yu, B.L.; Pacureanu, A.; Olivier, C.; Cloetens, P.; Peyrin, F. Assessment of the human lacuna-canalicular network at the nanoscale and impact of spatial resolution. *Sci. Rep.* **2020**, *10*, 4567.
44. Galkowski, V.; Petrisor, B.; Drew, B.; Dick, D. Bone stimulation for fracture healing: What's all the fuss. *Indian J. Orthop.* **2009**, *43*, 117–120.
45. Khalifeh, J.M.; Zohny, Z.; MacEwan, M.; Stephen, M.; Johnston, W.; Gamble, P.; Zeng, Y.; Yan, Y.; Ray, W.Z. Electrical stimulation and bone healing: A review of current technology and clinical applications. *IEEE Rev. Biomed. Eng.* **2018**, *11*, 217–232. [CrossRef]
46. Khare, D.; Basu, B.; Dubey, A.K. Electrical stimulation and piezoelectric biomaterials for bone tissue engineering applications. *Biomaterials* **2020**, *258*, 120280.
47. Sun, J.F.; Xie, W.Q.; Wu, Y.X.; Li, Z.; Li, Y. Accelerated bone healing via electrical stimulation. *Adv. Sci.* **2024**. *Epub ahead of print*. [CrossRef]
48. Hu, Y.; Li, X.; Zhao, Z.; Zhang, C.; Zhou, L.; Li, Y.; Liu, Y.; Wang, J.; Wang, Z.L. Triboelectric nanogenerator with low crest factor via precise phase difference design realized by 3D printing. *Small Methods* **2021**, *5*, e2100936. [CrossRef]
49. Jiang, D.J.; Ouyang, H.; Shi, B.J.; Zou, Y.; Tan, P.; Qu, X.; Chao, S.; Xi, Y.; Zhao, C.; Fan, Y.; et al. A wearable noncontact free-rotating hybrid nanogenerator for self-powered electronics. *InfoMat* **2020**, *2*, 1191–1200. [CrossRef]
50. Li, X.Y.; Xu, G.Q.; Xia, X.; Fu, J.; Huang, L.; Zi, Y. Standardization of triboelectric nanogenerators: Progress and perspectives. *Nano Energy* **2019**, *56*, 40–55. [CrossRef]

51. Zhao, Z.W.; Wen, S.M. Direct preparation of $CaTi_4(PO_4)_6$ coatings on the surface of Ti substrates by micro arc oxidation. *J. Mater. Sci. Mater. Med.* **2008**, *18*, 2275–2281. [CrossRef] [PubMed]
52. Ning, C.Y.; Zhou, L.; Tan, G.X. Fourth generation biomedical materials. *Mater. Today* **2015**, *19*, 193–200. [CrossRef]